BIOCHEMISTRY
including biophysical chemistry & molecular biology

Article

pubs.acs.org/biochemistry

Curvature Enhances Binding and Aggregation of Huntingtin at Lipid Membranes

Maxmore Chaibva,[†,‡] Kathleen A. Burke,[†] and Justin Legleiter*[,†,‡,§]

[†]The C. Eugene Bennett Department of Chemistry, West Virginia University, Morgantown, West Virginia 26505, United States
[‡]WVnanoSAFE, West Virginia University, Morgantown, West Virginia 26505, United States
[§]The Center for Neurosciences, West Virginia University, Morgantown, West Virginia 26505, United States

Supporting Information

ABSTRACT: Huntington disease (HD) is a genetic neurodegenerative disease caused by an expanded polyglutamine (polyQ) domain in the first exon of the huntingtin (Htt) protein, facilitating its aggregation. Htt interacts with a variety of membraneous structures within the cell, and the first 17 amino acids (Nt17) of Htt directly flanking the polyQ domain comprise an amphiphathic α-helix (AH) lipid-binding domain. AHs are also known to detect membrane curvature. To determine if Htt exon 1 preferentially binds curved membranes, in situ atomic force microscopy (AFM) studies were performed. Supported lipid bilayers are commonly used as model membranes for AFM studies of protein aggregation. However, these supported bilayers usually lack curvature. By forming a bilayer on top of silica nanobeads (50 ± 10 nm) deposited on a silicon substrate, model supported lipid bilayers with flat and curved regions were developed for AFM studies. The presence of the bilayer over the beads was validated by continual imaging of the formation of the bilayer, height measurements, and spatially resolved mechanical measurements of the resulting bilayer using scanning probe acceleration microscopy. Interpretation of this data was facilitated by numerical simulations of the entire imaging process. The curved supported bilayers associated with the beads were found to be more compliant than flat supported bilayers, consistent with the altered packing density of lipids caused by the induced curvature. This model bilayer system was exposed to a synthetic truncated Htt exon 1 peptide ($Nt17Q_{35}P_{10}KK$), and this peptide preferentially accumulated on curved membranes, consistent with the ability of AHs to sense membrane curvature.

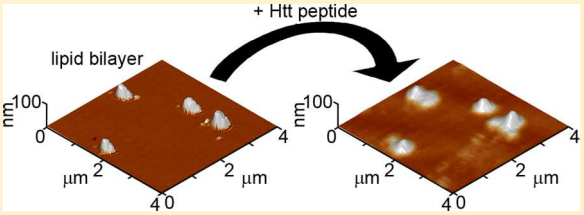

Huntington's disease, a fatal neurodegenerative disease, is caused by an expansion of a polyglutamine (polyQ) domain in the first exon of the huntingtin (Htt) protein.[1] Lying near the N-terminus of the protein, expansion of polyQ beyond a critical threshold (~35−39 repeat residues) directly leads to the formation of a variety of Htt aggregates (i.e., oligomers and fibrils), with the eventual formation of inclusion bodies in HD brain tissues.[2] The age of onset and severity of disease are strongly correlated with the length of the polyQ expansion.[3] Full-length Htt is over 3000 amino acids in size; however, a large number of truncated Htt products are produced in vivo via proteolysis,[4−6] and several lines of evidence suggest that the first exon of Htt may play an important role in HD. For example, the expression of Htt exon 1 with an expanded polyQ tract causes a progressive neurological phenotype in transgenic mice,[2,7] and N-terminal fragments comparable to exon 1 are detected in knock-in mouse models of HD that express full-length Htt[2,7] and in HD patients.[5]

Structural analysis of the first 17 amino acids of Htt exon 1 (Nt17) directly preceding the polyQ tract suggests that it functions as a lipid binding domain, as it forms an amphiphilic α-helix (AH).[8−10] The addition of Nt17 shifts the aggregation process of polyQ in free solution to a pathway that includes oligomeric intermediates.[11−13] Further studies suggest that surfaces, including lipid membranes, can further modulate the aggregation process, favoring the formation of amorphous accumulations of Htt exon 1 and small oligomers.[14,15] Targeting the Nt17 domain with other molecules is an effective way to alter Htt aggregation.[11,16] A polyproline (polyP) domain is directly adjacent to the C-terminal side of the polyQ domain in Htt. The polyP sequence also influences the aggregation kinetic as well as the aggregate conformational and structural properties of Htt.[17,18] The aggregation of Htt on model lipid membranes is also modulated by the presence of the polyP domain.[15]

Upon subcellular fractionation of neuron-like clonal striatal cells, ~50% of endogenous Htt partitions with membranes.[19] Association of Htt with lipids is further supported by the accumulation of lipid species in Htt aggregates observed in transgenic mouse models of HD.[20,21] Beyond playing a role in targeting lipid membranes, Nt17 functions to traffic Htt to the endoplasmic reticulum, mitochondria, Golgi, and various vesicles.[22−24] N-terminal fragments of Htt have been observed in membranes that were isolated from brain.[4] An apparent correlation between polyQ length and insertion into lipid membranes[14,25] suggests that Htt's interactions with lipids may

Received: December 4, 2013
Revised: March 1, 2014
Published: March 26, 2014

   dx.doi.org/10.1021/bi401619q | *Biochemistry* 2014, 53, 2355−2365

play a role in HD. In this regard, Htt has been shown to disrupt bilayer structure, altering the local mechanical properties of supported membranes.[14,26]

A variety of protein motifs play a critical role in sensing and targeting specific physical properties of membranes. In particular, membrane curvature is a physical property targeted by AHs.[27−29] Because the Nt17 domain of Htt has been shown to have an amphipathic helical structure as a monomer,[30] fibril,[12] and when bound to lipids,[9,10,12] we wanted to determine if Htt preferentially binds to curved membranes. In recent years, supported lipid bilayers have been increasingly used as model substrates for atomic force microscopy (AFM) studies aimed at understanding protein aggregation on membranes;[26,31−36] however, because these supported bilayers are typically flat, it is difficult to account for the potential role of membrane curvature in protien/lipid interaction using this method. Here, we developed and validated a system comprising a model supported lipid bilayer with both flat and curved regions. This system was exposed to a synthetic Htt peptide to determine if curvature plays a role in the interaction of Htt with lipid membranes. The model synthetic Htt peptide was chosen on the basis of several considerations: (1) 35 Q repeats in synthetic peptides are sufficient for aggregation,[13] (2) the polyP domain length (10 prolines) is similar to that directly adjacent to polyQ in Htt exon 1, (3) the known lipid-binding properties of Nt17,[22] and (4) this same peptide has been demonstrated to affect lipid membranes in a similar manner as the full Htt exon 1 protein.[15]

MATERIALS AND METHODS

Preparation of Supported Flat and Curved Bilayers. Lyophilized total brain lipid extract (TBLE) (Avanti Polar Lipids) was dissolved in chloroform (ACROS Organics). The chloroform was evaporated using a Vacufuge plus concentrator (Eppendorf) to form a thin lipid film on the bottom walls of a microcentrifuge tube. The TBLE was reconstituted in 10 mM Tris HCl buffer (pH 7.3) with periodic vortexing to a concentration of 1 mg/mL. To facilitate bilayer and multilayer sheet formation, the lipid sample tube went through five freeze/thaw cycles by sequential immersion in liquid nitrogen followed by thawing at 37 °C in a thermomixer (Eppendorf).[37] The lipid sample was then bath-sonicated for 45 min to facilitate vesicle formation. Fifteen microliters of 1:1 mixture of TBLE/Tris-HCl was added directly into an AFM fluid cell on a clean silicon substrate decorated with 50 nm silica nanoparticles (Polysciences, PA). The same lot of lipids was used in all experiments. TBLE contains a physiologically relevant ratio of membrane components and is composed of 9.6% phosphatidylcholine (PC), 16.7% phosphatidylethanolamine (PE), 1.6% phosphatidylinositol (PI), 10.6% phosphatidylserine (PS), 2.8% phosphatidic acid (PA), and 58.7% unknown (based on the product description on the Avanti Polar Lipids Web site).

Preparation of Poly-L-lysine-Coated Silicon Substrate. Ultraflat silicon wafers, type ⟨100⟩ (Ted Pella), were cut into 1 × 1 cm^2 squares and sequentially sonicated in acetone, absolute ethanol, and deionized water for 20 min each. The wafers were then kept under water overnight and dried with canned air. The clean substrates were placed under ozone for 1 h to remove any traces of organic contaminants[38] from the acetone and ethanol. Once more, the wafers were rinsed in ultrapure water, dried with air, and placed on a hot plate at 30 °C to remove any residual solvent present. These substrates were stored in a dust-free environment prior to use. A 25 μL aliquot of 0.1% poly-L-lysine was evenly spread on the clean, square silicon substrate, which was then placed on a hot plate at 30 °C for 5 min followed by rinsing with 1 mL of deionized water to remove excess unbound poly-L-lysine molecules.[39]

Nanoparticles Deposition on Silicon Substrate. Silica nanoparticles purchased from Polysciences were diluted to the desired concentration of 0.010% (0.10 g/L) with ultrapure water followed by 60 min of sonication prior to deposition. A 20 μL drop of the silica dispersion was evenly spread on the poly-L-lysine-coated silicon substrate and allowed to dry slowly at room temperature.[40] This was rinsed with 100 μL of ultrapure water to remove any excess, loosely bound beads on the surface, air-dried, and stored in a dust-free environment prior to AFM experiments.

In Situ AFM and SPAM Imaging Conditions. A Nanoscope V Multimode AFM (Veeco, Santa Barbara, CA) equipped with a tapping mode fluid cell and an O ring was used to perform in situ AFM experiments. The silicon substrates with beads were scanned using a rectangular-shaped silicon nitride cantilever (Vista Probes) with a nominal spring constant of 0.1 N/m and a tip radius of <10 nm. Typical scan rates ranged from 1 to 2 Hz, and drive frequencies of 5 to 6 kHz were used. For scanning probe acceleration microscopy (SPAM) analysis,[41] topography images were captured at a 512 × 128 pixel resolution. As the topography images were being captured, the cantilever deflection trajectories were simultaneously captured with a signal access module (Veeco) and CompuScope 14100 data acquisition card (Gage, Lachine, QC) at 2.5 MS/s and 14 bit resolution with a range of 2 V. The captured cantilever trajectories were filtered with a sliding-window Fourier transform-based harmonic comb filter, and the second derivatives of the filtered cantilever deflection trajectories were taken and multiplied by the effective mass, m_{eff}, of the cantilever to obtain the time-resolved-based tapping force between the tip and sample. A thermal tuning method[42] was performed in solution to obtain the actual spring constant and resonance frequency of the cantilever under experimental conditions, and this information was used to determine m_{eff}.

Quantitative Image Analysis. AFM image analysis was performed using the image processing toolbox of MatLab (MathWorks, Natick, MA) as described elsewhere.[43] In short, the physical dimensions of the beads were measured by (1) importing images into MatLab, (2) correcting the images for background curvature, (3) applying a height threshold to create a binary map of the surface that could be used to locate individual beads, and (4) implementing pattern-recognition algorithms to the binary map to locate beads and to measure specific features of each individual bead. The height was determined by finding the tallest pixel associated with the location of an individual bead, and the volume was determined by summing the volume associated with every pixel in the image that represented a bead, as determined by the binary image created by the height threshold. Each bead in an AFM image was given a unique identity so that comparisons of the same bead could be made from image to image. The increase in the total volume of a bead upon exposure to peptide was determined by subtracting the volume of individual, lipid-coated beads before exposure to peptide to the newly measured volume of the same bead as a function of time after the initial exposure to peptide. For most experiments, there were typically between 9 and 17 beads present in the area of surface being monitored. The total volume of protein deposited on flat regions of the bilayer was determined by use of the height

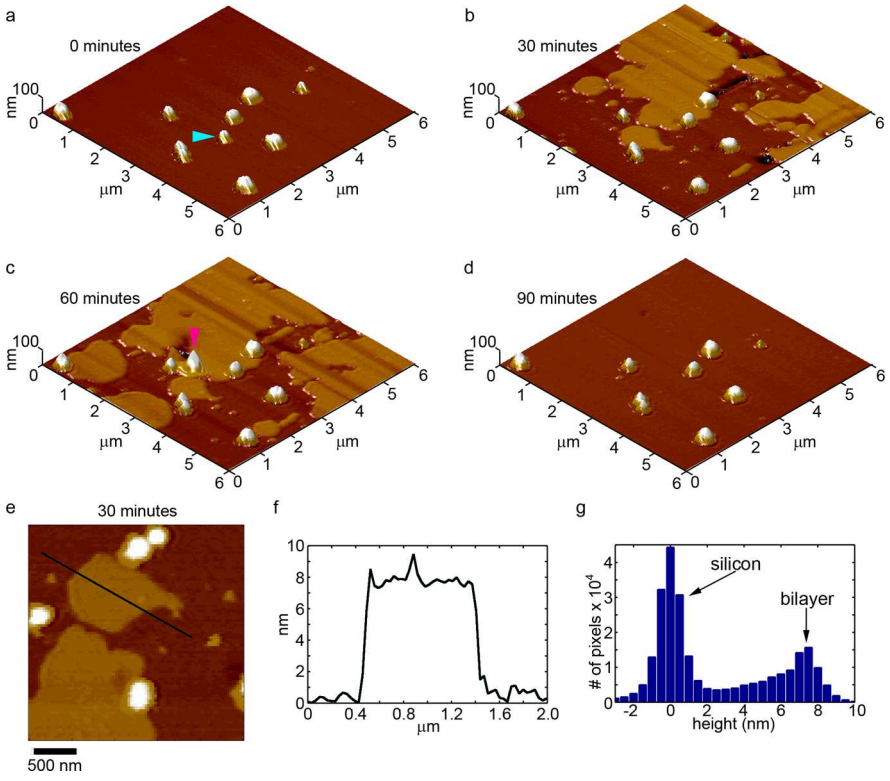

Figure 1. Time-lapse AFM images taken in solution of a TBLE bilayer forming over silica beads immobilized on silicon. Images were taken of the surface (a) before exposure to lipid vesicles and (b–d) at 30 min increments after injection of lipid vesicles. The blue arrow in panel a indicates a silica bead that was knocked off of the surface by the imaging process and does not appear in subsequent images. The red arrow in panel c indicates a lipid vesicle that did not completely flattened and fused into the bilayer. A zoomed-in AFM image was taken at (e) 30 min after injection of TBLE into the fluid cell with the black line corresponding to the (f) height profile. (g) Histogram of height measurements associated with each pixel in the image presented in panel e demonstrating the height of the bilayer.

threshold, removal of pixels associated with beads, dividing the image into 16 equally sized regions using a symmetrical grid, and summing the increase in volume associated with pixels above the threshold for each region. The same height threshold value (0.5 nm) was used for all measurements.

Numerical Simulations. To understand the tip/sample forces, we carried out numerical simulations in which the cantilever was modeled as a driven damped harmonic oscillator[44]

$$m_{\text{eff}}\ddot{z} + b\dot{z} + k[z - D_0 + a_0 \sin(\omega t)] = F_{\text{ext}} \quad (1)$$

where m_{eff} is the effective mass of the cantilever, b is the damping coefficient, k is the spring constant of the cantilever, z is the position of the cantilever with respect to the surface, a_0 is the drive amplitude, ω is the drive frequency, D_0 is the rest position of the cantilever base, and F_{ext} is the tip/sample force. During imaging with tapping mode AFM, the cantilever oscillation changes the separation distance between the tip and the sample surface, resulting in two force regimes: (1) noncontact forces when the tip and surface are not in contact and (2) tip/surface contact forces associated with the tapping event. The first force regime, when there is no tip/surface contact, was approximated by the van der Waals interaction between a sphere and a flat surface[45]

$$F_{\text{ext}} = -\frac{HR_{\text{tip}}}{6z^2} \text{ for } z > a_{\text{DMT}} \quad (2)$$

where H is the Hamaker constant, R_{tip} is the radius of the tip, z is the separation distance, and a_{DMT} is the interatomic distance parameter.[46] The tip/sample force associated with the tapping event can be modeled by a DMT potential

$$F_{\text{ext}} = \frac{4}{3\pi\kappa_{\text{eff}}}\sqrt{R}(a_{\text{DMT}} - z)^{3/2} - \frac{HR_{\text{tip}}}{6a_{\text{DMT}}^2} \text{ for } z \le a_{\text{DMT}} \quad (3)$$

with

$$\kappa_{\text{eff}} = \frac{1 - \upsilon_{\text{tip}}^2}{\pi E_{\text{tip}}} + \frac{1 - \upsilon_{\text{sample}}^2}{\pi E_{\text{sample}}} \quad (4)$$

where υ_{tip}, E_{tip} and υ_{sample}, E_{sample} are the Young's moduli and Poisson coefficients of the tip and sample, respectively.

To simulate the entire scanning process, the model was equipped with a feedback loop containing an integral gain. In actual atomic force microscopes, the cantilever deflection signal is monitored rather than the position with respect to the surface. Therefore, the feedback loop in the model monitored the oscillation amplitude of the cantilever deflection (y), which is related to the position by

$$y = z - D_0 + a_0 \sin(\omega t) \quad (5)$$

The amplitude of the deflection signal was directly compared to a set-point amplitude, and the distance between the cantilever and sample was adjusted to maintain the set-point amplitude. The feedback loop feature allowed for the simulation of the process of acquiring an AFM scan line with a specified topography.

dx.doi.org/10.1021/bi401619q | Biochemistry 2014, 53, 2355–2365

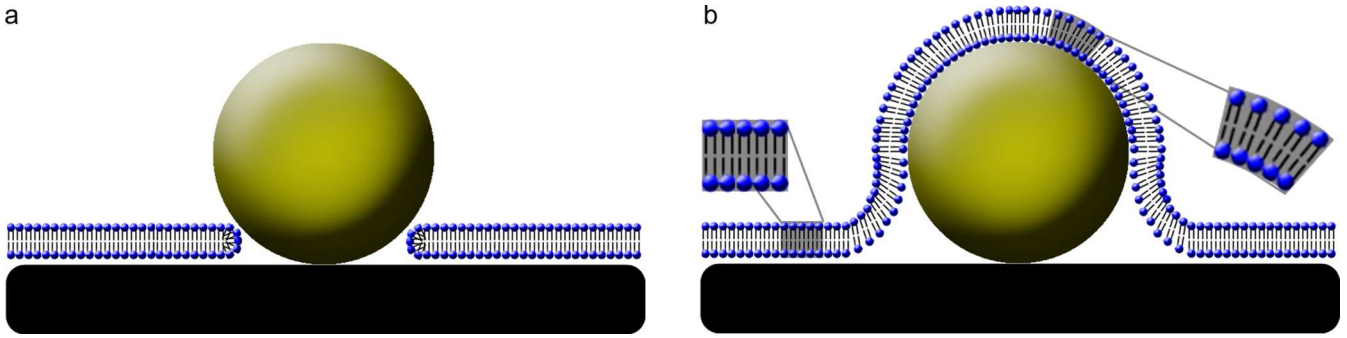

Figure 2. Schematics demonstrating two potential ways the lipid bilayer could be arranged with respect to the beads: (a) the bilayer could form along the surface but not over the bead or (b) the bilayer could form over the top of the bead, which would result in different packing associated with the forced geometry (insets).

Peptide Preparation. A synthetic peptide based on Htt exon 1, $Nt17Q_{35}P_{10}KK$, was obtained via custom synthesis (Keck Biotechnology Resource Laboratory, New Haven, CT). Disaggregation and solubilization of the peptide was achieved on the basis of established protocols.[47] Briefly, crude peptide was dissolved for 3 h in a 1:1 mixture of trifluoroacetic acid (Acros Organics) and hexafluoroisopropanol (Acros Organics) at a concentration of 0.5 mg/mL. Samples were rigorously vortexed, and the solvent was then evaporated off with a gentle stream of nitrogen. To remove any trace amounts of solvent from the peptide, samples were placed in a Vacufuge concentrator (Eppendorf). This process produced thin peptide films that were resuspended in ultrapure water adjusted to pH 3 with trifluoroacetic acid to 200 μM, snap frozen, and stored at −80 °C. These stock solutions were thawed and immediately diluted with 10 mM Tris-HCl buffer (Fisher Scientific) to a final concentration of 20 μM and with a resulting pH of 7.3.

RESULTS

Development of a System Containing Supported Curved and Flat Lipid Bilayers. To provide a substrate capable of inducing well-defined, local regions of curvature in a supported bilayer, the strategy of using silica beads (diameter of 50 ± 10 nm) that were immobilized on clean silicon surfaces pretreated with 0.1% poly-L-lysine as substrates was employed (Figure 1a). These substrates were subsequently exposed to vesicles composed of TBLE, resulting in the formation of a lipid bilayer on the surface via the process of vesicles flattening and fusing on the surface (Figure 1b−c). This strategy provided both curved and flat bilayers in the same system and allowed for the direct tracking of Htt aggregation on these two distinct regions by AFM imaging in solution. Although the beads were found to be firmly attached to the surface, the process of acquiring AFM images and/or injecting solutions containing vesicle into the fluid cell did result in rare instances in which a bead was displaced from the surface (Figure 1a, blue arrow). The formation of the lipid bilayer on the flat portions of the substrate could be tracked by continuous AFM imaging of the scan area, and a smooth bilayer completely covered these flat regions of the surface typically within ~90 min. At intermediate time points, the thickness of the bilayer could be determined from analysis of AFM height images. The supported bilayer above the flat silicon substrate was 7.3 ± 0.4 nm, as demonstrated by height profiles and histograms of the height associated with every pixel in the image (Figure 1e−g). This observed height for the TBLE bilayer was surprising, as our previous work using the same lipid system on mica resulted in a bilayer height of ~3.5 to 4 nm.[37,48] This extra height may reflect contributions to the height associated with the poly-L-lysine layer used to immobilize the beads on the silicon surface.

Despite the obvious formation of lipid bilayer on the flat portions of the substrate, there are two primary ways the bilayer can form to accommodate the presence of the immobilized bead: (1) by forming a pore around the periphery of the bead or (2) by forming a bilayer over the top of the bead and thus enveloping it (Figure 2). Both scenarios have been observed in the literature.[40] The first scenario is not useful for this study, as it would not result in a curved model bilayer; however, the second scenario would provide such a surface. As a result, the formation of the bilayer forming over the top of the beads, and thus encapsulating them, needed to be verified. Previous studies used a comparison of the height of the bead and phase imaging before and after addition of lipid to determine if the bilayer formed over the bead.[40] The logic behind this approach is that if the bilayer forms on the flat substrate and on top of the bead then there would be no apparent change in height of the bead. If the bilayer formed a pore around the bead, then the observed bead height would be decreased by the thickness of the bilayer. Therefore, the average height of the exact same beads immobilized on the silicon surface was compared before addition of any lipid and after the bilayer appeared to have completely covered the flat portions of the substrate. There was an observed decrease of 2.9 ± 0.6 nm in the average bead height associated with the presence of the lipid bilayer. This was measured by comparing the measured height of individual beads before and after the formation of a bilayer. Because the bilayer on the flat region was known to have an average height of 7.3 nm, this smaller observed height suggests not only that some form of lipid did indeed deposit over the top of the beads but also that there is something physically different between the lipid on top of the bead and the flat portion of the substrate.

Validating Bilayer Formation on Beads Using Imaging Forces. To provide an understanding of why this small height difference was observed and to validation further that a bilayer had indeed formed over the top of the bead, analysis of the time-resolved imaging forces associated with tapping mode AFM was performed. These imaging forces have been demonstrated to be highly dependent on surface mechanical properties, and in particular, the maximum tapping force (F_{max}), defined as the peak or largest force occurring between the tip and surface during a single tapping event, can be used as an indirect measure of the compression or Young's modulus of a sample. As AFM topography images were obtained of the beads on silicon before and after the formation of a lipid bilayer, the

dx.doi.org/10.1021/bi401619q | Biochemistry 2014, 53, 2355−2365

entire cantilever deflection signal was captured and processed to recover the time-resolved tip/sample tapping force by SPAM. In this way, the tapping forces can be associated with specific features in the topography image and used to make surface maps of mechanical properties. To aid in interpreting these force maps and to relate them directly to the observed height measurements of the beads, several numerical simulations of the complete tapping mode AFM imaging process in solution were performed as described in the Materials and Methods.[26,37,49]

The rigidity of a surface can be modeled by varying the Young's modulus of the sample in eq 4. A series of simulations were run with Young's modulus values of the model surface ranging from 0.5 to 100 GPa (Figure 3). All other imaging parameters were held constant (i.e., cantilever free amplitude, spring constant, and set-point ratio) when imaging these model surfaces. As a result, the total tip/sample imaging force over an entire cantilever oscillation cycle was constant; however, this force was distributed differently over the entire tapping event (Figure 3a). As the surface became increasingly more compliant, the contact time between the tip and surface increased, resulting in the imaging force being distributed over this longer contact time with a corresponding decrease in the F_{max} associated with the tapping event. This decrease in F_{max} with smaller values of surface Young's modulus followed a power law dependence (Figure 3b). For any given set of imaging parameters, this power law dependence between F_{max} and the surface Young's modulus was observed, although the magnitude of the forces would vary. For example, increasing the cantilever spring constant resulted in larger values of F_{max}, but for any given spring constant, the power law dependence between F_{max} and Young's modulus was observed (Figure 3b). This demonstrates that for any given set of imaging parameters F_{max} can be used as a way to compare the relative rigidity of features within an AFM image.

Next, numerical simulations of imaging a bead deposited on a surface via tapping mode AFM in solution were performed. The model surface used in these simulations was 125 nm long and contained a 50 nm wide curved region that was 50 nm in height and flanked by flat regions (Figure 4a). The Young's modulus of the flat and curved regions of the model surface could be independently altered. First, simulations were performed to determine if changes in F_{max} could be potentially associated with the curvature associated with the beads. When the Young's moduli of the flat and curved regions of the model surface were equal, there was no observed change in F_{max} (Figure 4b). When the Young's moduli differed between the flat and curved regions, F_{max} changed, as would be predicted on the basis of the power law dependence, that is, the softer region was always associated with a smaller F_{max} regardless of whether this corresponded to the flat or curved region. Next, the measured

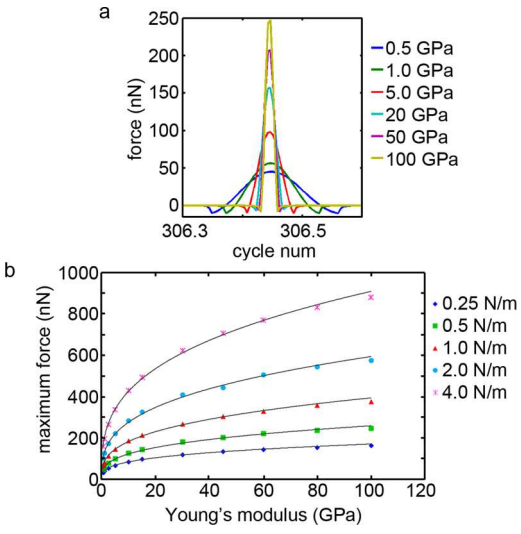

Figure 3. Tapping mode AFM simulations demonstrate the relationship between imaging forces and surface mechanical properties. (a) Simulated time-resolved tip/sample forces associated with tapping mode AFM imaging on surfaces with various values of Young's modulus. (b) Maximum tapping force as a function of the surface Young's modulus for cantilevers with different spring constants.

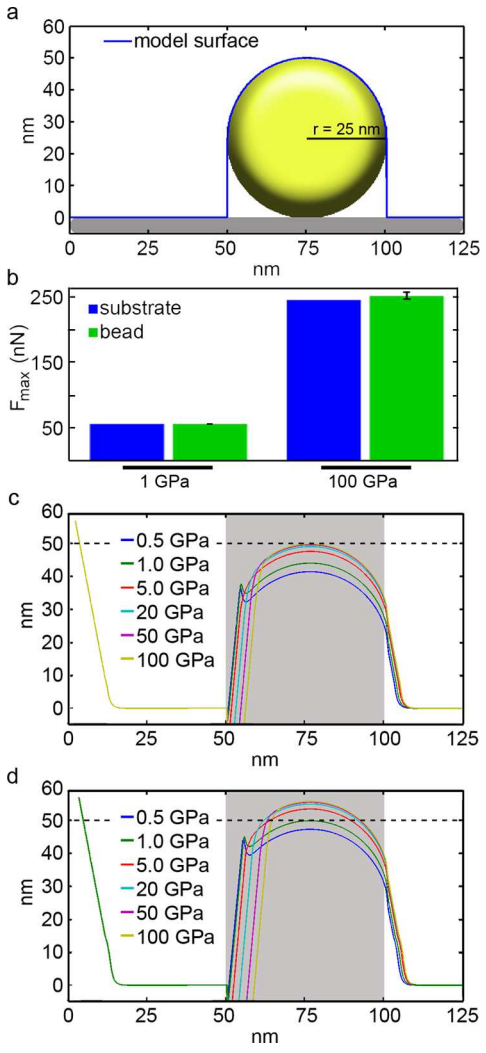

Figure 4. Tapping mode AFM simulations demonstrate the effect of Young's modulus on the measured height of a 50 nm bead. (a) Model surface used in these simulations consisted of a 125 nm long surface that contained a 50 nm bead (radius of 25 nm). (b) Comparison of F_{max} associated with flat and curved substrates of the same Young's modulus. (c) Simulated height traces of a bead with different values of Young's modulus sitting on a substrate with a Young's modulus of 100 GPa. (d) Simulated height traces of a bead with different values of Young's modulus sitting on a substrate with a Young's modulus of 1 GPa. In both panels c and d, the location of the bead is highlighted with gray shading, and the true bead height is indicated by the dashed line.

dx.doi.org/10.1021/bi401619q | *Biochemistry* 2014, 53, 2355−2365

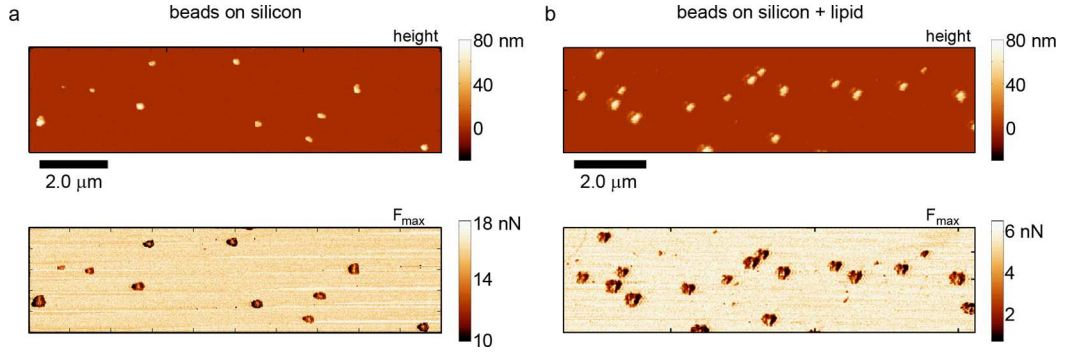

Figure 5. Maximum forces associated with imaging the surfaces confirm the presence of lipid bilayers covering the beads. Height and the corresponding F_{max} images of beads deposited on silicon substrates (a) before addition of lipid vesicles and (b) after the formation of a lipid bilayer are presented. There is a small double-tip imaging artifact in the AFM image shown in panel b.

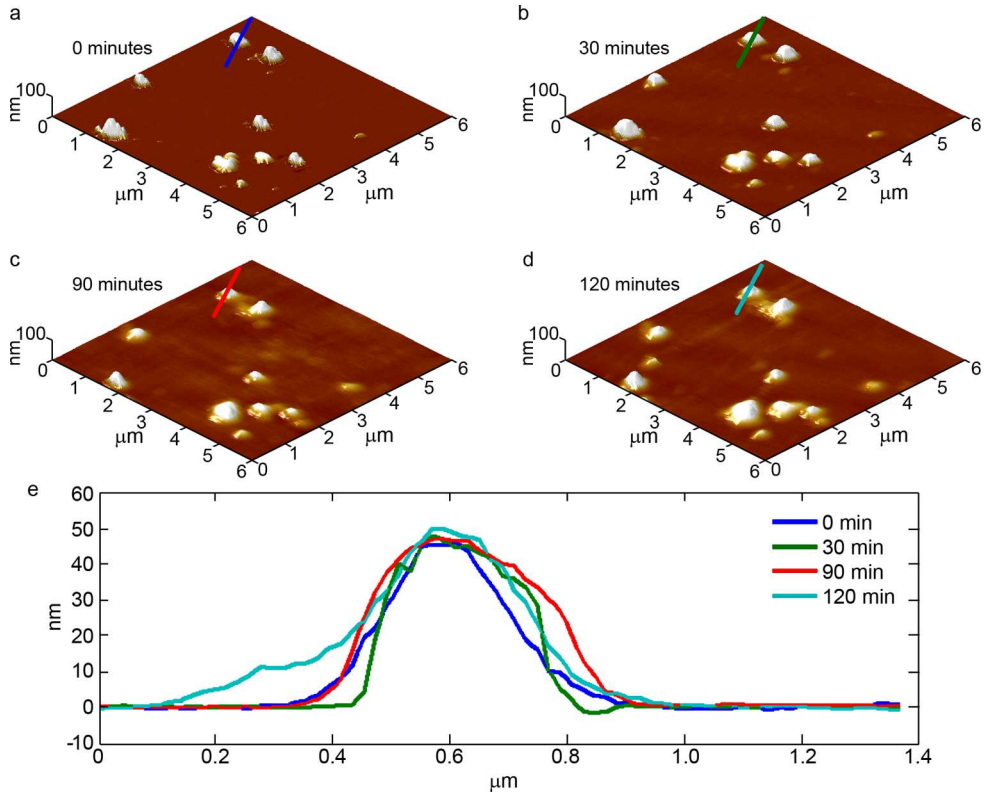

Figure 6. Time-lapse AFM images taken in solution of a TBLE bilayer exposed to a synthetic Htt exon 1-mimicking peptide ($Nt17Q_{35}P_{10}KK$). Images were taken of the surface (a) before exposure to $Nt17Q_{35}P_{10}KK$ and (b–d) at 30 min increments after injection of the peptide. The colored lines in each image correspond to (e) cross-sections of the same bead.

height of the model bead with varying values of Young's modulus (ranging from 0.5 to 100 GPa) with respect to the flat region of the surface, which had a Young's modulus of 100 (Figure 4c) or 1.0 GPa (Figure 4d), was determined. When the bead and flat regions of the model surface had the same Young's modulus, the measured height of the bead was the same as the true height of the bead (i.e., 50 nm). Whenever the flat region of the model surface was more rigid compared to the bead, the observed height was smaller compared to the true height of the bead, with the observed height becoming increasingly smaller with lower values of Young's modulus. If the flat portion of the surface was softer than the bead, then the observed height of the bead became systematically larger than the true height as the Young's modulus of the bead increased. The deviation of the height of the bead from the true height is a result of the applied force associated with the imaging process compressing the softer regions of the surface to a greater extent, which forms the basis of compliance-based contrast in AFM.

Keeping the results of the AFM simulations in mind, to confirm the presence of a lipid bilayer on top of the beads, the relative local rigidity of actual surfaces was mapped before and after the formation of the lipid bilayer. This was accomplished by reconstructing the time-resolved tip/sample force associated with every tapping event while obtaining AFM images by SPAM, allowing F_{max} (and thus rigidity) to be correlated to specific regions of the surface. There was stark contrast in the F_{max} image between beads and bare silicon (Figure 5). The magnitude of the force indicated that the beads were softer compared to the bare substrate, which is consistent with the literature values of Young's moduli of the two materials. The

dx.doi.org/10.1021/bi401619q | *Biochemistry* 2014, 53, 2355–2365

bulk Young's modulus of silica is ~73 GPa, and the Young's modulus of silicon is typically >100 GPa. After a bilayer was observed to form completely on the flat portion of the substrate, the magnitude of F_{max} corresponding to the location of the beads was smaller than the surrounding bilayer. Because supported lipid bilayers have a Young's modulus on the order of 1 GPa or smaller, the F_{max} associated with an exposed silica bead would be larger. Thus, the observed F_{max} suggests that a lipid bilayer covered the beads and that the curved bilayers on top of beads were more compliant (smaller Young's modulus) than the flat supported bilayers. On the basis of the simulations, the increased compliance resulted in a smaller measured height of the bead because the tip compressed the curved bilayer to a larger extent compared to the flat bilayer. The reduced Young's modulus of bilayers on top of the beads was most likely a result of altered packing of the lipid components because of the induced curvature (Figure 2b, insets).

Htt Peptides Preferentially Bind to Curved Bilayers. After establishing that the substrates supported both curved and flat regions of bilayer, these bilayers were exposed to a synthetic truncated Htt exon 1 peptide ($Nt17Q_{35}P_{10}KK$) (Figure 6). This peptide contained a 35-residue long polyQ domain flanked by the lipid-binding Nt17 domain and a 10-residue long polyP domain. Two lysines were added at the C-terminus of the peptide to aid solubility.[47] Observations were limited to regions of the bilayer that were confirmed to be completely covered by lipid bilayer, as determined by AFM analysis, prior to exposure to $Nt17Q_{35}P_{10}KK$. The addition of $Nt17Q_{35}P_{10}KK$ indicated our zero time point for exposure, and no additional protein was added after this initial injection. For each experiment, $Nt17Q_{35}P_{10}KK$ was freshly prepared and was in a predominately monomeric state upon initial injection, although some small aggregates were most likely present. Control experiments exposing TBLE bilayers to protein-free vehicle solvents were performed, and no observable morphological changes in the bilayer were associated with the injection of vehicle, as assessed by AFM.

The binding and aggregation of $Nt17Q_{35}P_{10}KK$ on the bilayer surface was tracked by AFM imaging for 120 min (Figure 6). The portions of the surface occupied by beads visibly swelled within 30 min of exposure to $Nt17Q_{35}P_{10}KK$ as peptide accumulated on the curved bilayers, and these curved regions continued to expand in volume with time. The increase in volume associated with the curved regions of the substrate occurred uniformly, as all curved regions appeared to be accumulating peptide. The accumulation of peptide by the curved bilayers predominately occurred in the lateral dimension, as an increase in the width of the regions associated with beads grew more quickly in comparison with the height (see example cross-sections as a function of time in Figure 6e).

The flat regions of the bilayer exhibited morphological changes (i.e., became rougher) in discrete regions within the first 30 min of exposure; however, unperturbed regions of the bilayer were still observed. With time, the area of the perturbed regions on the flat bilayers expanded, and the roughness increased, which is indicative of Htt binding, aggregating, and disrupting the bilayer. The height scale of the images presented in Figure 6 was optimized to demonstrate the binding of $Nt17Q_{35}P_{10}KK$ to the curved bilayers. Although a hint of the bilayer roughening can be observed in these images, adjusting the color map demonstrates this more clearly (Figure 7). A freshly formed bilayer on the flat portion of the substrate has a smooth appearance with an rms roughness typically less than

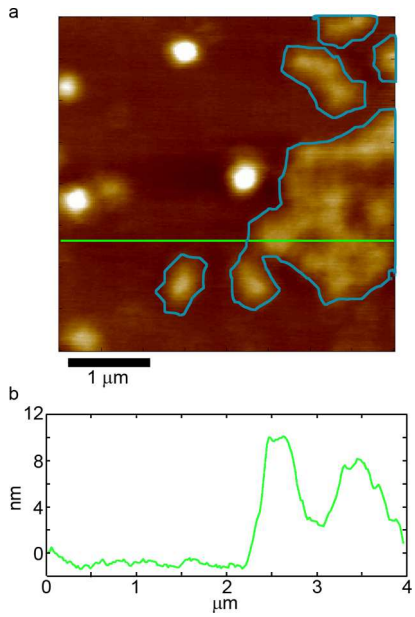

Figure 7. (a) AFM image with adjusted height contrast shows that a synthetic Htt exon 1-mimicking peptide ($Nt17Q_{35}P_{10}KK$) aggregates on and disrupts the flat regions of the lipid bilayer. This image was taken 90 min after the initial exposure to the Htt peptide. The regions indicated by blue perimeters have increased surface roughness associated with the binding and aggregation of $Nt17Q_{35}P_{10}KK$. The green line in the image corresponds to the height profile in panel b.

0.2 nm. Exposure to $Nt17Q_{35}P_{10}KK$ resulted in patches of increased surface roughness on the flat lipid bilayer, consistent with disruption of the bilayer structure by binding of the peptide. The rms roughness of these regions exceeds 0.5 nm, and the roughness increases with time as more peptide binds and/or aggregates in these regions.

To quantify and compare the total amount of $Nt17Q_{35}P_{10}KK$ that bound to the curved and the flat regions of the bilayer, the total volume change of the different regions was determined by AFM image analysis. Because the flat regions of the bilayer represented a significantly larger surface area of the substrate, the change in volume was normalized per unit area. The initial volume of each lipid-covered bead before exposure to $Nt17Q_{35}P_{10}KK$ was subtracted for each subsequent measurement to determine the increase in volume of each individual bead. Simulations of tip convolution[50] associated with AFM imaging of model beads that systematically increased in volume were performed to determine the expected error associated with the finite size and shape of the tip in determining the volume of deposited peptide (see the Supporting Information for a complete description). These simulations indicated that although tip convolution caused the measured volume to be typically overestimated, this error never exceeded 15%. The increased volume associated with flat regions of the bilayer was measured by summing the volume of the features observed above the baseline of the unperturbed bilayer height. Through both of these measurements, the volume associated with the initial deposition of the bilayer was controlled for both the curved and flat regions of the surface. On the basis of this analysis, $Nt17Q_{35}P_{10}KK$ preferentially accumulated on the curved rather than the flat regions of the bilayer, even when taking into account the potential 15% overestimation because of tip convolution of the beads (Figure 8). Although $Nt17Q_{35}P_{10}KK$ accumulated on both types of surface,

dx.doi.org/10.1021/bi401619q | Biochemistry 2014, 53, 2355−2365

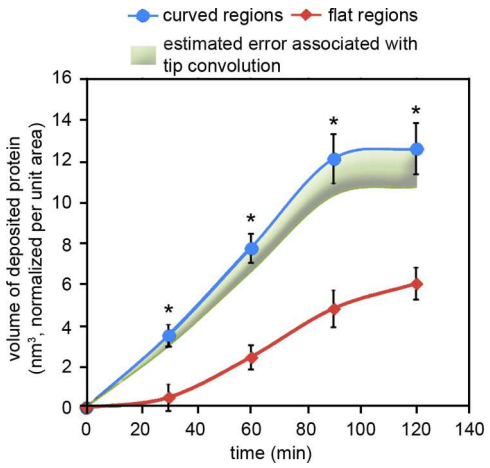

Figure 8. Volume of deposited synthetic Htt exon 1–mimicking peptide ($Nt17Q_{35}P_{10}KK$) on the curved or flat regions of the bilayer. The shaded region represents the estimated volume of peptide deposited on the curved bilayers after taking into account tip convolution (percent error assumed to be ≤15% based on simulations described in the Supporting Information).

significant differences ($p < 0.05$) in the volume of the deposited peptide were observed within 30 min. The amount of deposited peptide increased linearly for the next hour for both regions of the bilayer; however, the accumulation of peptide occurred more rapidly on the curved regions. After ∼90 min, accumulation of peptide on the curved bilayer appeared to level off.

DISCUSSION

Although tapping mode AFM in solution is widely used to study the morphological and mechanical properties of supported lipid bilayers, one of the limitations associated with comparing these results to physiologically relevant membranes is the lack of membrane curvature associated with such systems. A potential method to induce curvature in supported lipid membranes is to introduce local curvature in the substrate. Here, we accomplished this by depositing silica nanobeads onto a silicon substrate, and by the process of vesicle fusion, we formed a supported lipid bilayer that covered the flat silicon substrate and curved beads. Verification of the lipid bilayer forming on top of the beads was provided by a combination of height measurements and analysis of time-resolved tip/sample forces. Interpretation of both height and force analysis was aided by numerical simulations of the entire imaging process involving a model surface of the correct topography. Interestingly, F_{max} revealed that not only did lipid organize on top of the beads but also that bilayers on top of the beads had a qualitative reduction in the Young's modulus compared to a bilayer supported by flat regions of the substrate, which was consistent with alterations in lipid packing associated with induced curvature.[51,52] Collectively, these results demonstrate that membrane curvature can significantly alter bilayer mechanical properties and that these changes can be detected by AFM tip/sample force reconstruction.

With the validation that supported lipid bilayers formed over the beads, we had a model system that allowed us to monitor the interaction of proteins with curved or flat regions of a bilayer simultaneously. There are several advantages associated with such an approach. Force measurements confirmed that the bilayer on top of the beads was mechanically, and thus structurally, different compared to the flat portions of the bilayer. Although we chose to use TBLE as our lipid system, this approach should be amenable to various lipid systems. Because of the uniform size of the beads, the curved portions of the supported bilayer are relatively uniform. In theory, the curvature can be modified by changing the size of the beads; however, encapsulation of immobilized beads by a lipid bilayer does not occur on all bead sizes, as has been previously observed.[40,53] This reinforces the importance of confirming the formation of the bilayer over the top of the beads. Another caveat associated with this approach that should be noted is that these bilayers are still supported and that underlying substrates may influence the fluidity and other properties of lipid membranes.

When exposing these model bilayers to freshly prepared solutions of an N-terminal Htt fragment, we found that the peptide preferentially accumulated on curved regions of the bilayer. Although Htt fragments with expanded polyQ domains are predominately found in nuclear or cytoplasmic inclusion bodies,[7] Htt also directly associates with numerous membranous surfaces, such as mitochondria, endoplasmic reticulum (ER), tubulovesicles, endosomes, lysosomes, and synaptic vesicles, within the cell.[2,54] Although the size of mitochondria and ER are larger than the size of the beads used to model curvature in this study, tubulovesicles, endosomes, lysosomes, and synaptic vesicles can have diameters on the order of 50 nm,[55−57] providing some physiological relevance to this model system. The environments provided by these membrane surfaces could influence the aggregation of Htt with expanded polyQ domains, and these membranous structures exhibit varying degrees of curvature. This curvature may provide nucleation sites for aggregation by creating local areas of high Htt concentration because of enhanced binding. The accumulation of monomeric Htt and/or prefibrillar aggregates directly binding lipid membranes has been shown to disrupt bilayer integrity and to induce mechanical changes in the membrane.[14,15,26]

Beyond these implications of Htt/lipid interactions in disease mechanisms, there are several membrane-associated functions attributable to Htt in which the lipid-binding properties of Nt17 may play a role. Some of these functions include Htt functioning in cellular adhesion,[58] motility,[59,60] cholesterol and energy homeostasis,[61] and as a molecular scaffold for coordination of membrane and cytoskeletal communication[8] as well as facilitating micrutobule-dependent vesicle transport.[62] Nt17 facilitates the trafficking of Htt exon 1 to membranes associated with the ER, autophagic vacuoles, mitochondria, and Golgi.[22,23] Membrane curvature sensing by the Nt17 domain of Htt may represent a mechanistic detail of some of these functions, and disruption of these normal lipid-associated functions of Htt may play a role in toxicity associated with expanded polyQ domains. Supporting the notion that Nt17 directly interacts with lipid membranes, the binding of Htt exon 1 to large unilamellar vesicles composed of PC or a mixture of PC and PS alters the helical content of Nt17, and the associated changes in helical content could be inhibited by the addition of a proline at the eighth residue of Nt17.[22] Structural studies utilizing solid-state NMR suggest that Nt17 has a predominantly random-coil structure in solution and adopts its α-helical structure upon binding lipid bilayers.[9,10] Furthermore, the presence of Nt17 in synthetic polyQ peptides was necessary to bind model TBLE membranes and to induce leakage of TBLE vesicles.[15]

One potential mechanism to explain how Nt17, which is an AH, preferentially binds curved membranes is that bilayer curvature introduces a high density of membrane defects that can act as binding sites. AHs represent a common motif in a variety of proteins to sense membrane curvature.[27−29] The insertion process of AHs may be facilitated by lipid packing defects induced by membrane curvature, resulting in a larger number of potential binding sites for the protein.[28,63,64] Assuming that the lipid mass is conserved on both leaflets of a lipid bilayer and that the lipid composition of the bilayer remains constant, the density of defects within the leaflet of a bilayer associated with positive curvature would increase with bending.[29] Once a Htt monomer (or possibly a small aggregate) binds to the lipid membrane, this creates a site where more Htt could preferentially accumulate through interaction with the immobilized peptide. This could explain the rapid, amorphous deposition of peptide associated with the curved bilayer regions. This notion is further supported by previous observations that monomeric Htt exon 1 proteins preferentially accumulate onto immobilized preformed aggregates[65] and that Htt exon 1 tends to alter the morphology of lipid bilayers in discrete regions that grow in size with time.[14,15] These discrete regions of disruption on the flat portions of the bilayer were also observed in this study.

It is also possible that the curvature induced by the bilayer skewed the distribution of specific lipid components of the TBLE. That is, specific lipid components may preferentially accumulated around the beads. The AFM images presented here do not provide evidence that this selective enrichment of lipid components associated with the bead occurred; however, such phenomena are well-known in several biological membrane systems.[66] If specific lipid components of TBLE were enriched over the beads, then perhaps a higher affinity of Htt for these specific lipid components contributes to its preference for curved membranes, as Htt has been shown to interact preferentially with a variety of lipid components.[67] These two potential mechanisms, defect detection or higher affinity for enriched lipid components, are not mutually exclusive and both may contribute to Htt's preference for the curved membrane. However, experimental and modeling studies have demonstrated that the selectivity of AHs for curved membranes is dominated by increases in binding sites (packing defects) rather than increases in binding affinity (lipid enrichment).[29] The binding of amyloid-forming proteins to membrane defects via AHs has been demonstrated for other amyloid-forming proteins, such as α-synuclein[64,68] and islet amyloid polypeptide.[69]

Several other factors can potentially play a role in regulating the interaction of Htt exon 1 fragments facilitated by Nt17 with lipid membranes. For example, several residues in Nt17 can undergo post-translational modifications, such as phosphorylation, acetylation, and SUMOlyation, and some of these modifications have been shown to regulate the interaction of Htt with specific organelles.[22,70] Additional affinity-based components for the interaction of other AHs with lipid bilayers have been experimentally observed. Such considerations include electrostatics,[71,72] partitioning of lipid components,[73−75] or the presence of other specific recognition motifs.[76,77] In particular, electrostatic mechanisms likely play a role in Htt/lipid interactions, as Htt binds multivalent phosphatidylinsoitol phospates (PIPs) and has a high affinity for cardiolipin.[25,67]

■ ASSOCIATED CONTENT

Supporting Information

Description of the geometric model used for estimating the error associated with measuring the volume of beads associated with tip convolution; effect of tip convolution on the observed volume of a bead; and percent error associated with our method for determining the increase in volume of a bead. This material is available free of charge via the Internet at http://pubs.acs.org.

■ AUTHOR INFORMATION

Corresponding Author

*E-mail: justin.legleiter@mail.wvu.edu; Telephone: 304-293-0175.

Funding

This work was supported by the National Science Foundation (NSF no. CMMI1054211) and the WV Higher Education Policy Commission/Division of Science and Research.

Notes

The authors declare no competing financial interest.

■ REFERENCES

(1) The Huntington's Disease Collaborative Research Group (1993) A novel gene containing a trinucleotide repeat that is expanded and unstable on Huntington's disease chromosomes. *Cell 72*, 971−983.

(2) DiFiglia, M., Sapp, E., Chase, K. O., Davies, S. W., Bates, G. P., Vonsattel, J. P., and Aronin, N. (1997) Aggregation of huntingtin in neuronal intranuclear inclusions and dystrophic neurites in brain. *Science 277*, 1990−1993.

(3) Ravina, B., Romer, M., Constantinescu, R., Biglan, K., Brocht, A., Kieburtz, K., Shoulson, I., and McDermott, M. P. (2008) The relationship between CAG repeat length and clinical progression in Huntington's disease. *Mov. Disord. 23*, 1223−1227.

(4) Kim, Y. J., Yi, Y., Sapp, E., Wang, Y. M., Cuiffo, B., Kegel, K. B., Qin, Z. H., Aronin, N., and DiFiglia, M. (2001) Caspase 3-cleaved N-terminal fragments of wild-type and mutant huntingtin are present in normal and Huntington's disease brains, associate with membranes, and undergo calpain-dependent proteolysis. *Proc. Natl. Acad. Sci. U.S.A. 98*, 12784−12789.

(5) Ratovitski, T., Gucek, M., Jiang, H., Chighladze, E., Waldron, E., D'Ambola, J., Hou, Z., Liang, Y., Poirier, M. A., Hirschhorn, R. R., Graham, R., Hayden, M. R., Cole, R. N., and Ross, C. A. (2009) Mutant huntingtin N-terminal fragments of specific size mediate aggregation and toxicity in neuronal cells. *J. Biol. Chem. 284*, 10855−10867.

(6) Ratovitski, T., Nakamura, M., D'Ambola, J., Chighladze, E., Liang, Y., Wang, W., Graham, R., Hayden, M. R., Borchelt, D. R., Hirschhorn, R. R., and Ross, C. A. (2007) N-terminal proteolysis of full-length mutant huntingtin in an inducible PC12 cell model of Huntington's disease. *Cell Cycle 6*, 2970−2981.

(7) Davies, S. W., Turmaine, M., Cozens, B. A., DiFiglia, M., Sharp, A. H., Ross, C. A., Scherzinger, E., Wanker, E. E., Mangiarini, L., and Bates, G. P. (1997) Formation of neuronal intranuclear inclusions underlies the neurological dysfunction in mice transgenic for the HD mutation. *Cell 90*, 537−548.

(8) Kegel, K. B., Sapp, E., Yoder, J., Cuiffo, B., Sobin, L., Kim, Y. J., Qin, Z. H., Hayden, M. R., Aronin, N., Scott, D. L., Isenberg, F., Goldmann, W. H., and DiFiglia, M. (2005) Huntingtin associates with acidic phospholipids at the plasma membrane. *J. Biol. Chem. 280*, 36464−36473.

(9) Michalek, M., Salnikov, E. S., and Bechinger, B. (2013) Structure and topology of the huntingtin 1−17 membrane anchor by a combined solution and solid-state NMR approach. *Biophys. J. 105*, 699−710.

(10) Michalek, M., Salnikov, E. S., Werten, S., and Bechinger, B. (2013) Membrane interactions of the amphipathic amino terminus of huntingtin. *Biochemistry 52*, 847−858.
(11) Jayaraman, M., Kodali, R., Sahoo, B., Thakur, A. K., Mayasundari, A., Mishra, R., Peterson, C. B., and Wetzel, R. (2012) Slow amyloid nucleation via alpha-helix-rich oligomeric intermediates in short polyglutamine-containing huntingtin fragments. *J. Mol. Biol. 415*, 881−899.
(12) Sivanandam, V. N., Jayaraman, M., Hoop, C. L., Kodali, R., Wetzel, R., and van der Wel, P. C. A. (2011) The aggregation-enhancing huntingtin N-terminus is helical in amyloid fibrils. *J. Am. Chem. Soc. 133*, 4558−4566.
(13) Thakur, A. K., Jayaraman, M., Mishra, R., Thakur, M., Chellgren, V. M., Byeon, I.-J. L., Anjum, D. H., Kodali, R., Creamer, T. P., Conway, J. F., Gronenborn, A. M., and Wetzel, R. (2009) Polyglutamine disruption of the huntingtin exon 1 N terminus triggers a complex aggregation mechanism. *Nat. Struct. Mol. Biol. 16*, 380−389.
(14) Burke, K. A., Hensal, K. M., Umbaugh, C. S., Chaibva, M., and Legleiter, J. (2013) Huntingtin disrupts lipid bilayers in a polyQ-length dependent manner. *Biochim. Biophys. Acta, Biomembr. 1828*, 1953−1961.
(15) Burke, K. A., Kauffman, K. J., Umbaugh, C. S., Frey, S. L., and Legleiter, J. (2013) The interaction of polyglutamine peptides with lipid membranes is regulated by flanking sequences associated with huntingtin. *J. Biol. Chem. 288*, 14993−15005.
(16) Mishra, R., Jayaraman, M., Roland, B. P., Landrum, E., Fullam, T., Kodali, R., Thakur, A. K., Arduini, I., and Wetzel, R. (2012) Inhibiting the nucleation of amyloid structure in a huntingtin fragment by targeting alpha-helix-rich oligomeric intermediates. *J. Mol. Biol. 415*, 900−917.
(17) Bhattacharyya, A., Thakur, A. K., Chellgren, V. M., Thiagarajan, G., Williams, A. D., Chellgren, B. W., Creamer, T. P., and Wetzel, R. (2006) Oligoproline effects on polyglutamine conformation and aggregation. *J. Mol. Biol. 355*, 524−535.
(18) Darnell, G., Orgel, J. P., Pahl, R., and Meredith, S. C. (2007) Flanking polyproline sequences inhibit beta-sheet structure in polyglutamine segments by inducing PPII-like helix structure. *J. Mol. Biol. 374*, 688−704.
(19) Kegel, K. B., Kim, M., Sapp, E., McIntyre, C., Castano, J. G., Aronin, N., and DiFiglia, M. (2000) Huntingtin expression stimulates endosomal-lysosomal activity, endosome tubulation, and autophagy. *J. Neurosci. 20*, 7268−7278.
(20) Suopanki, J., Gotz, C., Lutsch, G., Schiller, J., Harjes, P., Herrmann, A., and Wanker, E. E. (2006) Interaction of huntingtin fragments with brain membranes − clues to early dysfunction in Huntington's disease. *J. Neurochem. 96*, 870−884.
(21) Valencia, A., Reeves, P. B., Sapp, E., Li, X. Y., Alexander, J., Kegel, K. B., Chase, K., Aronin, N., and DiFiglia, M. (2010) Mutant huntingtin and glycogen synthase kinase 3-beta accumulate in neuronal lipid rafts of a presymptomatic knock-in mouse model of Huntington's disease. *J. Neurosci. Res. 88*, 179−190.
(22) Atwal, R. S., Xia, J., Pinchev, D., Taylor, J., Epand, R. M., and Truant, R. (2007) Huntingtin has a membrane association signal that can modulate huntingtin aggregation, nuclear entry and toxicity. *Hum. Mol. Genet. 16*, 2600−2615.
(23) Rockabrand, E., Slepko, N., Pantalone, A., Nukala, V. N., Kazantsev, A., Marsh, J. L., Sullivan, P. G., Steffan, J. S., Sensi, S. L., and Thompson, L. M. (2007) The first 17 amino acids of huntingtin modulate its sub-cellular localization, aggregation and effects on calcium homeostasis. *Hum. Mol. Genet. 16*, 61−77.
(24) Trettel, F., Rigamonti, D., Hilditch-Maguire, P., Wheeler, V. C., Sharp, A. H., Persichetti, F., Cattaneo, E., and MacDonald, M. E. (2000) Dominant phenotypes produced by the HD mutation in STHdh(Q111) striatal cells. *Hum. Mol. Genet. 9*, 2799−2809.
(25) Kegel, K. B., Schewkunow, V., Sapp, E., Masso, N., Wanker, E. E., DiFiglia, M., and Goldmann, W. H. (2009) Polyglutamine expansion in huntingtin increases its insertion into lipid bilayers. *Biochem. Biophys. Res. Commun. 387*, 472−475.
(26) Burke, K. A., Yates, E. A., and Legleiter, J. (2013) Amyloid-forming proteins alter the local mechanical properties of lipid membranes. *Biochemistry 52*, 808−817.
(27) Drin, G., and Antonny, B. (2010) Amphipathic helices and membrane curvature. *FEBS Lett. 584*, 1840−1847.
(28) Drin, G., Casella, J.-F., Gautier, R., Boehmer, T., Schwartz, T. U., and Antonny, B. (2007) A general amphipathic alpha-helical motif for sensing membrane curvature. *Nat. Struct. Mol. Biol. 14*, 138−146.
(29) Hatzakis, N. S., Bhatia, V. K., Larsen, J., Madsen, K. L., Bolinger, P.-Y., Kunding, A. H., Castillo, J., Gether, U., Hedegard, P., and Stamou, D. (2009) How curved membranes recruit amphipathic helices and protein anchoring motifs. *Nat. Chem. Biol. 5*, 835−841.
(30) Kim, M. W., Chelliah, Y., Kim, S. W., Otwinowski, Z., and Bezprozvanny, I. (2009) Secondary structure of huntingtin amino-terminal region. *Structure 17*, 1205−1212.
(31) Drolle, E., Gaikwad, R. M., and Leonenko, Z. (2012) Nanoscale electrostatic domains in cholesterol-laden lipid membranes create a target for amyloid binding. *Biophys. J. 103*, L27−L29.
(32) Hane, F., Drolle, E., and Leonenko, Z. (2010) Effect of cholesterol and amyloid-β peptide on structure and function of mixed-lipid films and pulmonary surfactant BLES: An atomic force microscopy study. *J. Nanomed. Nanotechnol. 6*, 808−814.
(33) Legleiter, J., Fryer, J. D., Holtzman, D. M., and Kowalewski, T. (2011) The modulating effect of mechanical changes in lipid bilayers caused by ApoE-containing lipoproteins on Abeta induced membrane disruption. *ACS Chem. Neurosci. 2*, 588−599.
(34) Yates, E. A., Owens, S. L., Lynch, M. F., Cucco, E. M., Umbaugh, C. S., and Legleiter, J. (2013) Specific domains of Abeta facilitate aggregation on and association with lipid bilayers. *J. Mol. Biol. 425*, 1915−1933.
(35) Yip, C. M., Darabie, A. A., and McLaurin, J. (2002) Abeta42-peptide assembly on lipid bilayers. *J. Mol. Biol. 318*, 97−107.
(36) Yip, C. M., Elton, E. A., Darabie, A. A., Morrison, M. R., and McLaurin, J. (2001) Cholesterol, a modulator of membrane-associated Abeta-fibrillogenesis and neurotoxicity. *J. Mol. Biol. 311*, 723−734.
(37) Shamitko-Klingensmith, N., Molchanoff, K. M., Burke, K. A., Magnone, G. J., and Legleiter, J. (2012) Mapping the mechanical properties of cholesterol-containing supported lipid bilayers with nanoscale spatial resolution. *Langmuir 28*, 13411−13422.
(38) Sundh, M., Svedhem, S., and Sutherland, D. S. (2011) Formation of supported lipid bilayers at surfaces with controlled curvatures: Influence of lipid charge. *J. Phys. Chem. B 115*, 7838−7848.
(39) Zhang, W., Hughes, J., and Chen, Y. (2012) Impacts of hematite nanoparticle exposure on biomechanical, adhesive, and surface electrical properties of *Escherichia coli* cells. *Appl. Environ. Microbiol. 78*, 3905−3915.
(40) Roiter, Y., Ornatska, M., Rammohan, A. R., Balakrishnan, J., Heine, D. R., and Minko, S. (2008) Interaction of nanoparticles with lipid membrane. *Nano Lett. 8*, 941−944.
(41) Legleiter, J., Park, M., Cusick, B., and Kowalewski, T. (2006) Scanning probe acceleration microscopy (SPAM) in fluids: Mapping mechanical properties of surfaces at the nanoscale. *Proc. Natl. Acad. Sci. U.S.A. 103*, 4813−4818.
(42) Hutter, J. L., and Bechhoefer, J. (1993) Calibration of atomic-force microscope tips. *Rev. Sci. Instrum. 64*, 1868−1873.
(43) Burke, K. A., Godbey, J., and Legleiter, J. (2011) Assessing mutant huntingtin fragment and polyglutamine aggregation by atomic force microscopy. *Methods 53*, 275−284.
(44) Kuhle, A., Sorensen, A. H., and Bohr, J. (1997) Role of attractive forces in tapping tip force microscopy. *J. Appl. Phys. 81*, 6562−6569.
(45) Israelachvili, J. N. (1991) *Intermolecular and Surface forces*, Academic Press, London.
(46) Derjaguin, B. V., Muller, V. M., and Toporov, Y. P. (1975) Effect of contact deformations on the adhesion of particles. *J. Colloid Interface Sci. 53*, 314−326.
(47) Chen, S. M., and Wetzel, R. (2001) Solubilization and disaggregation of polyglutamine peptides. *Protein Sci. 10*, 887−891.
(48) Kumar, B., Pifer, P. M., Giovengo, A., and Legleiter, J. (2010) The effect of set point ratio and surface Young's modulus on

maximum tapping forces in fluid tapping mode atomic force microscopy. *J. Appl. Phys. 107*, 044508-1−044508-8.
(49) Legleiter, J., and Kowalewski, T. (2005) Insights into fluid tapping-mode atomic force microscopy provided by numerical simulations. *Appl. Phys. Lett. 87*, 163120-1−163120-3.
(50) Villarrubia, J. S. (1997) Algorithms for scanned probe microscope image simulation, surface reconstruction, and tip estimation. *J. Res. Natl. Inst. Stand. Tehcnol. 102*, 425−454.
(51) Vamparys, L., Gautier, R., Vanni, S., Bennett, W. F. D., Tieleman, D. P., Antonny, B., Etchebest, C., and Fuchs, P. F. J. (2013) Conical lipids in flat bilayers induce packing defects similar to that induced by positive curvature. *Biophys. J. 104*, 585−593.
(52) Vanni, S., Vamparys, L., Gautier, R., Drin, G., Etchebest, C., Fuchs, P. F. J., and Antonny, B. (2013) Amphipathic lipid packing sensor motifs: Probing bilayer defects with hydrophobic residues. *Biophys. J. 104*, 575−584.
(53) Roiter, Y., Ornatska, M., Rammohan, A. R., Balakrishnan, J., Heine, D. R., and Minko, S. (2009) Interaction of Lipid Membrane with Nanostructured Surfaces. *Langmuir 25*, 6287−6299.
(54) Gutekunst, C. A., Li, S. H., Yi, H., Mulroy, J. S., Kuemmerle, S., Jones, R., Rye, D., Ferrante, R. J., Hersch, S. M., and Li, X. J. (1999) Nuclear and neuropil aggregates in Huntington's disease: Relationship to neuropathology. *J. Neurosci. 19*, 2522−2534.
(55) Cataldo, A. M., Barnett, J. L., Pieroni, C., and Nixon, R. A. (1997) Increased neuronal endocytosis and protease delivery to early endosomes in sporadic Alzheimer's disease: Neuropathologic evidence for a mechanism of increased β-amyloidogenesis. *J. Neurosci. 17*, 6142−6151.
(56) Osawa, W., and Ogata, T. (1978) Scanning electron-microscopic study on fractured rat parietal-cells in resting state and after stimulation with tetragastrin. *Arch. Histol. Jpn. 41*, 141−155.
(57) Qu, L., Akbergenova, Y., Hu, Y., and Schikorski, T. (2009) Synapse-to-synapse variation in mean synaptic vesicle size and its relationship with synaptic morphology and function. *J. Comp. Neurol. 514*, 343−352.
(58) Strehlow, A. N., Li, J. Z., and Myers, R. M. (2007) Wild-type huntingtin participates in protein trafficking between the Golgi and the extracellular space. *Hum. Mol. Genet. 16*, 391−409.
(59) Ritch, J. J., Valencia, A., Alexander, J., Sapp, E., Gatune, L., Sangrey, G. R., Sinha, S., Scherber, C. M., Zeitlin, S., Sadri-Vakili, G., Irimia, D., DiFiglia, M., and Kegel, K. B. (2012) Multiple phenotypes in Huntington disease mouse neural stem cells. *Mol. Cell. Neurosci. 50*, 70−81.
(60) Myre, M. A., Lumsden, A. L., Thompson, M. N., Wasco, W., MacDonald, M. E., and Gusella, J. F. (2011) Deficiency of huntingtin has pleiotropic effects in the social amoeba *Dictyostelium discoideum*. *PLoS Genet. 7*, e1002052-1−e1002052-17.
(61) Jacobsen, J. C., Gregory, G. C., Woda, J. M., Thompson, M. N., Coser, K. R., Murthy, V., Kohane, I. S., Gusella, J. F., Seong, I. S., MacDonald, M. E., Shioda, T., and Lee, J. M. (2011) HD CAG-correlated gene expression changes support a simple dominant gain of function. *Hum. Mol. Genet. 20*, 2846−2860.
(62) Caviston, J. P., and Holzbaur, E. L. (2009) Huntingtin as an essential integrator of intracellular vesicular trafficking. *Trends Cell Biol. 19*, 147−155.
(63) Cornell, R. B., and Taneva, S. G. (2006) Amphipathic helices as mediators of the membrane interaction of amphitropic proteins, and as modulators of bilayer physical properties. *Curr. Protein Pept. Sci. 7*, 539−552.
(64) Nuscher, B., Kamp, F., Mehnert, T., Odoy, S., Haass, C., Kahle, P. J., and Beyer, K. (2004) Alpha-synuclein has a high affinity for packing defects in a bilayer membrane − A thermodynamics study. *J. Biol. Chem. 279*, 21966−21975.
(65) Legleiter, J., Mitchell, E., Lotz, G. P., Sapp, E., Ng, C., DiFiglia, M., Thompson, L. M., and Muchowski, P. J. (2010) Mutant Huntingtin fragments form oligomers in a polyglutamine length-dependent manner in vitro and in vivo. *J. Biol. Chem. 285*, 14777−14790.
(66) Hanzal-Bayer, M. F., and Hancock, J. F. (2007) Lipid rafts and membrane traffic. *FEBS Lett. 581*, 2098−2104.
(67) Kegel-Gleason, K. B. (2013) Huntingtin interactions with membrane phospholipids: Strategic targets for therapeutic intervention? *J. Huntington's Dis. 2*, 239−250.
(68) Davidson, W. S., Jonas, A., Clayton, D. F., and George, J. M. (1998) Stabilization of alpha-synuclein secondary structure upon binding to synthetic membranes. *J. Biol. Chem. 273*, 9443−9449.
(69) Caillon, L., Lequin, O., and Khemtemourian, L. (2013) Evaluation of membrane models and their composition for islet amyloid polypeptide-membrane aggregation. *Biochim. Biophys. Acta, Biomembr. 1828*, 2091−2098.
(70) Xia, J. R., Lee, D. H., Taylor, J., Vandelft, M., and Truant, R. (2003) Huntingtin contains a highly conserved nuclear export signal. *Hum. Mol. Genet. 12*, 1393−1403.
(71) McLaughlin, S., and Murray, D. (2005) Plasma membrane phosphoinositide organization by protein electrostatics. *Nature 438*, 605−611.
(72) Yeung, T., Gilbert, G. E., Shi, J., Silvius, J., Kapus, A., and Grinstein, S. (2008) Membrane phosphatidylserine regulates surface charge and protein localization. *Science 319*, 210−213.
(73) Linder, M. E., and Deschenes, R. J. (2007) Palmitoylation: Policing protein stability and traffic. *Nat. Rev. Mol. Cell Bio. 8*, 74−84.
(74) Manneville, J.-B., Casella, J.-F., Ambroggio, E., Gounon, P., Bertherat, J., Bassereau, P., Cartaud, J., Antonny, B., and Goud, B. (2008) COPI coat assembly occurs on liquid-disordered domains and the associated membrane deformations are limited by membrane tension. *Proc. Natl. Acad. Sci. U.S.A. 105*, 16946−16951.
(75) Rocks, O., Peyker, A., Kahms, M., Verveer, P. J., Koerner, C., Lumbierres, M., Kuhlmann, J., Waldmann, H., Wittinghofer, A., and Bastiaens, P. I. H. (2005) An acylation cycle regulates localization and activity of palmitoylated Ras isoforms. *Science 307*, 1746−1752.
(76) Lemmon, M. A. (2008) Membrane recognition by phospholipid-binding domains. *Nat. Rev. Mol. Cell Bio. 9*, 99−111.
(77) McMahon, H. T., and Gallop, J. L. (2005) Membrane curvature and mechanisms of dynamic cell membrane remodelling. *Nature 438*, 590−596.